



Universiteit
Leiden
The Netherlands

Dark ice chemistry in interstellar clouds

Qasim, D.N.

Citation

Qasim, D. N. (2020, June 30). *Dark ice chemistry in interstellar clouds*. Retrieved from <https://hdl.handle.net/1887/123114>

Version: Publisher's Version

License: [Licence agreement concerning inclusion of doctoral thesis in the Institutional Repository of the University of Leiden](#)

Downloaded from: <https://hdl.handle.net/1887/123114>

Note: To cite this publication please use the final published version (if applicable).

Cover Page



Universiteit Leiden



The handle <http://hdl.handle.net/1887/123114> holds various files of this Leiden University dissertation.

Author: Qasim, D.

Title: Dark ice chemistry in interstellar clouds

Issue Date: 2020-06-30

Dark ice chemistry in the laboratory

In this chapter, a general overview of the experimental setups used in this thesis to investigate the ‘dark’ ice chemistry in translucent and dense interstellar molecular clouds is provided. This includes a summary of the apparatus, SURFFace REaction SIMulation DEvice (SURFRESIDE), and the construction of an experimental apparatus complementary to the science on SURFRESIDE. Additionally, fundamental background knowledge, such as the mathematical details behind the analytical techniques used in SURFRESIDE, are described.

2.1 Experimental Setup: SURFRESIDE³

For over a decade, SURFRESIDE has been continuously upgraded to better probe the solid-state reactions that occur in the darkness of dense interstellar clouds (i.e., regions that are largely shielded by at least external UV photons), as well as in translucent clouds. As discussed in Chapter 1, these regions contain icy dust grains that are initially formed largely by the accretion of atoms. To mimic this process in the laboratory, SURFRESIDE is equipped with several state-of-the-art equipment, called atomic beamlines, that can produce intense beams with specific atoms. This includes a Hydrogen Atom Beam Source (HABS; see Fuchs et al. (2009)), an atomic H, N, O microwave atom source (MWAS; see Ioppolo et al. (2013)), and a C-atom source (Qasim et al. 2020b). Thus, the setup is currently labeled as SURFRESIDE³ to represent the 3 atomic beamlines. These beamlines are necessary if one wants to investigate the kinetics of formation and destruction, derive abundances, and/or disentangle the formation routes in the ices of interstellar clouds.

Due to the topic of study, the experiments investigated in this thesis solely involve the reaction between radicals and between radicals and small molecules (i.e., to mimic the reaction between simple species and without an ‘energetic’ source). All of the presented experiments occur in an ultrahigh vacuum (UHV) environment, as necessary to prevent the interference of atmospheric leak contamination. UHV is also necessary to prohibit uncontrolled reactions with water, which is a relatively abundant background gas. Since our ices have thicknesses as that of interstellar ices (< 100 monolayers, ~50 monolayers; 1 monolayer = 1×10^{15} molecules cm^{-2}), assuming a sticking coefficient of unity, it takes 45 minutes for 1 monolayer of contamination to grow on the surface in a

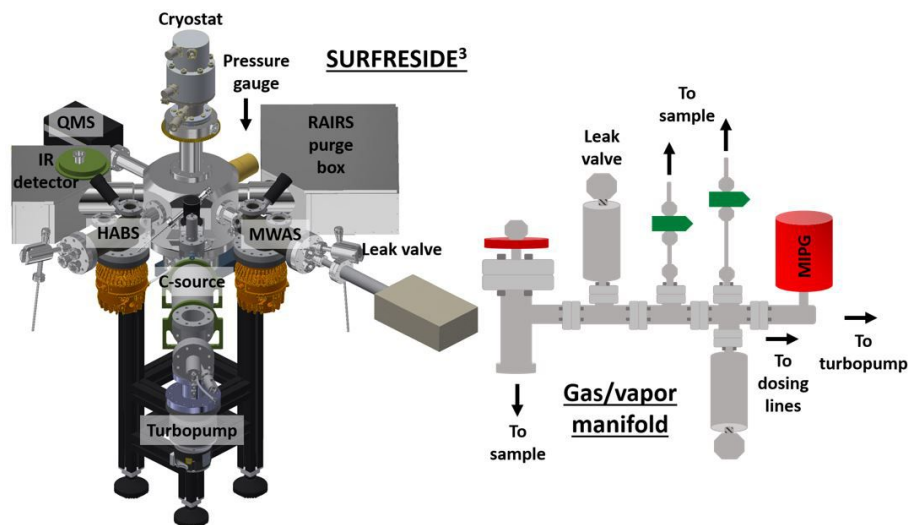


Figure 2.1: (Left) The experimental setup, SURFRESIDE³, used in this thesis. Image credit: M. Witlox. (Right) The gas manifold that is attached to the setup, which allows gases and vapors to enter the chamber(s).

chamber pressurized at 1.3×10^{-9} mbar (Harrison 2013). Therefore, a pressure of $< 1.3 \times 10^{-9}$ mbar (i.e., UHV pressure) is needed to have a clean ice mixture when growing thin (< 100 monolayers) ices.

Figure 2.1 displays the experimental setup (left) and gas manifold (right). Many of the details of the atomic beamlines incorporated into SURFRESIDE, as well as the other components of the setup, are available in Ioppolo et al. (2013), Chuang (2018, Univ. Leiden), and Qasim et al. (2020b). A closed-cycle helium cryostat (CH-204 SF), coupled with a compressor (HC-4E1), is used to cool the substrate to a base temperature of 7 K. The substrate is where the interstellar ice analogues are grown, and has an inert gold coating. It is inert so that only the ice chemistry is studied (i.e., the reaction of gold and ice is irrelevant to interstellar ice chemistry). The purpose of the gold coating is to create a reflective surface that is required to monitor spectroscopically the formation of the ices over time. Note that the ices formed have thicknesses that prohibit noticeable effects of the surface on the ice chemistry. A cartridge heater is used to heat the sample to a maximum temperature of 450 K, in which sapphire rods are used to prevent damage to the cryocooler. The sample is placed at the center of the main chamber, which reaches a base pressure of low 10^{-10} mbar prior to deposition, as measured by a cold cathode pressure gauge (Pfeiffer Vacuum, IKR270). Analytical tools include a Fourier Transform Infrared Spectrometer (FTIR; Agilent Cary 640/660) and a quadrupole mass spectrometer (QMS; Spectra Microvision Plus LM76). For the IR pathway (discussed in section 2.1.1), boxes purged with filtered compressed air are needed to remove gaseous H_2O and CO_2 .

The atomic beamline chambers, which are connected to the main chamber, are discussed below. The HABS (Tschersich & Von Bonin 1998; Tschersich 2000; Tschersich et al. 2008) includes a filament, which thermally breaks apart

H₂ molecules into H-atoms, and is placed inside a UHV chamber (average base pressure of low 10⁻¹⁰ mbar at room temperature). H₂ gas is introduced into the HABS by a leak valve, and is prepared in a turbomolecularly pumped dosing line. The MWAS (Oxford Scientific Ltd.) uses electrons, excited by a frequency of 2.45 GHz at a typical power of 275 W, to break apart molecules into fragments. An average base pressure of low 10⁻⁹ mbar is found, and gases are introduced into the MWAS chamber also by a leak valve, which is connected to a turbomolecularly pumped dosing line. To collisionally cool the radicals produced by both beamlines, a nose-shaped quartz pipe is attached at both exit channels. The carbon atom source (SUKO-A 40, from Dr. Eberl MBE-Komponenten GmbH (MBE)) chamber reaches an average base pressure of low 10⁻⁹ mbar. It consists of a tantalum filament that is packed with graphite powder, and is resistively heated during operation. Thus, a dosing line for the C-atom source chamber is not required. However, a new filament is required usually after ~14 hours of operation, and therefore a mini UHV gate valve is incorporated to separate the C-atom source from the main chamber. All three atomic chambers are attached to a water cooling shroud to prevent surrounding components from melting.

The gas/vapor manifold shown in Figure 2.1 is commonly used to prepare the gases/vapors that will enter the main chamber. Like the other gas lines, the manifold is turbomolecularly pumped. Vapors are admitted by an ultratorr connection (see Figure 2.1 manifold drawing, far left with red valve handle), and gases are entered via 1/4" Swagelok (green valves). A mass independent pressure gauge ("MIPG" in Figure 2.1, Pfeiffer Vacuum, CMR361) is used to monitor the pressure, which is useful since calibration for the mass of the gas is not required. This gauge spans from 0.1 and 1100 mbar, and therefore a Pirani transmitter (Pfeiffer Vacuum, TPR280) is also attached in order to probe the pressure down to 10⁻⁴ mbar (i.e., to ensure that the manifold is effectively pumped). Metal leak valves are used to separate gases within the manifold, and also to minimize leak contamination. Finally, the manifold is connected to two separate dosing lines that are connected to the main chamber by two separate leak valves.

2.1.1 Analytical techniques

Reflection-absorption Infrared Spectroscopy (RAIRS):

The basic principle of infrared (IR) absorption spectroscopy is that the energy of the incoming light must be equivalent to the energy gap between two vibrational states (i.e., resonant frequencies). The way in which a molecule vibrates is known as its vibrational "mode", and in order for a mode to be IR active, a change in the dipole moment of vibration must be induced when transitioning between the ground to the excited vibrational state. This is mathematically described below (Humblot & Pradier 2011):

$$\text{Signal intensity} \propto |\Psi_f^* E \mu_{fi} \Psi_i|^2 \quad (1)$$

where Ψ_f and Ψ_i stand for final and initial states, respectively, E is the electric field vector, and μ_{fi} is the transition dipole moment. RAIRS is a branch of IR spectroscopy which probes the absorption features of the adsorbed molecules.

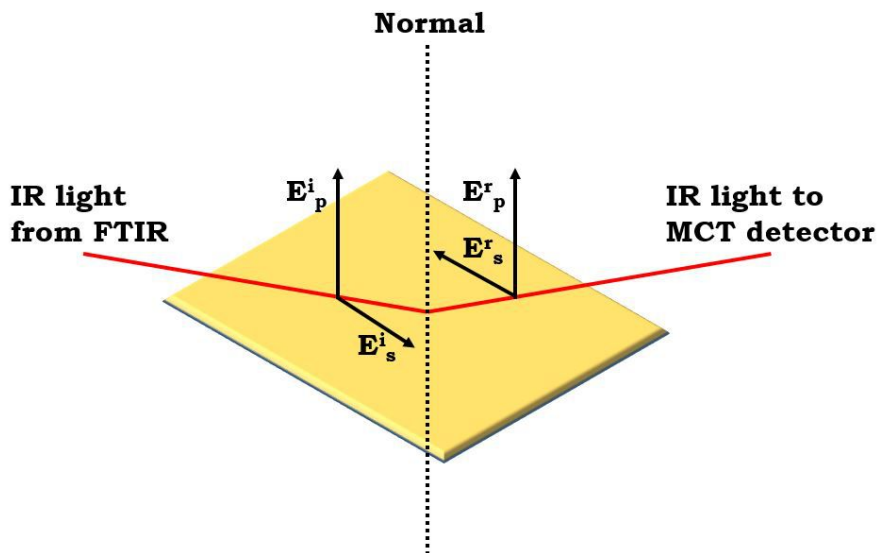


Figure 2.2: The s- and p-components of the electromagnetic field at the surface in a typical RAIRS study. Figure adapted from Humblot & Pradier (2011). On top of this surface is where ices are grown and probed.

It is surface sensitive and comes with an additional selection rule. Figure 2.2 provides a visual of the IR beam pathway when employing the RAIRS technique.

On SURFRESIDE³, IR light is emitted from a FTIR (allowed spectral range of 6000-700 cm^{-1} and a typically used resolution of 1 cm^{-1}), where it is focused onto the sample by external optics at $\sim 80^\circ$ to surface normal. This light is composed of two electric field vectors, namely s- and p-polarized. S-polarized gives rise to the longitudinal optical (LO) mode feature, and p-polarized additionally gives rise to the transverse optical (TO) mode feature (Palumbo et al. 2006). As shown in Figure 2.2, the s-component is parallel to the plane of the surface, and the p-component is orthogonal. The s-component of light is essentially negligible, and can be explained by the equation below (Humblot & Pradier 2011):

$$E_s = E_s^i [\sin\theta + r_s \sin(\theta + \delta_s)] \quad (2)$$

where E^i is the incident electric field at the surface, θ is an arbitrary phase angle, r is the reflection coefficient, and δ is the phase change. At all angles of incidence, δ is near 180° and r is close to unity (Humblot & Pradier 2011), making the electric field at the surface for the s-component close to zero. The p-component of light is split further into parallel and perpendicular components. As the incident and reflected parallel components are opposite in direction, the electric field contribution from the parallel component is negligible. The electric field of the perpendicular component of the p-component of light is described below (Humblot & Pradier 2011):

$$E_{p\perp} = E_p^i \sin\phi [\sin\theta + r_p \sin(\theta + \delta_p)] \quad (3)$$

where ϕ is the angle of incidence. As ϕ approaches 90° to surface normal, the electric field intensity increases until at 90° , in which the increasing δ_p leads to destructive interference. This leads to about $17\text{-}25\times$ increase in the sensitivity in comparison to transmission experiments when the grazing incidence angle is just below 90° (Friedbacher & Bubert 2011). Thus, RAIRS is advantageous in comparison to transmission IR in regards to its sensitivity.

In this thesis, RAIRS is particularly exploited to confirm the formation of reaction products *in situ* typically at a substrate temperature of 10 K. There are several ways in which RAIRS alone can be used to identify the species formed. However, it should be noted that for the identification of COMs, RAIRS alone typically cannot be used to secure a detection, as the probability of similar vibrational signatures increases as the molecular complexity increases. As each functional group has a vibrational mode that has a characteristic band strength (units of cm molecule^{-1} , see in the work by Bouilloud et al. (2015)), the relative intensities between the infrared features of the same molecule can be considered a diagnostic tool. As molecules have also different desorption temperatures, the temperature range at which the infrared peaks decrease can further constrain the identity of the species. Finally, according to Hooke's law, a heavier isotope will lead to a red-shift in the vibrational frequency. Thus, isotopic substitution can confirm the target functional group.

RAIRS also has the advantage of determining the amount of product formed by using a modified Lambert-Beer equation:

$$N = \frac{\ln 10 \cdot \int \text{Abs}(\nu) d(\nu)}{A'} \quad (4)$$

where N is the column density (molecule cm^{-2}), $\text{Abs}(\nu)d(\nu)$ is the change in absorbance (cm^{-1}), and A' is the band strength. These values are multiplied by $\ln(10)$ to convert to optical depth scale, since the spectrometer yields values in absorbance. Particularly for RAIRS experiments, the band strength is the more difficult parameter to obtain, since band strengths are typically measured by transmission IR in the literature. There are two ways in which band strengths are determined in this thesis: 1) The values are taken from laser interference measurements performed on SURFRESIDE by Chuang et al. (2018) and 2) a transmission-to-RAIR proportionality factor is used, in which the band strength of CO (2142 cm^{-1}) from the laser interference experiment performed by Chuang et al. (2018) is included.

Temperature Programmed Desorption (TPD):

A complementary technique to RAIRS is temperature programmed desorption (TPD). It is a well-established method that is regularly used in laboratory astrophysical ice and classical surface science experiments. Particularly in this thesis, the TPD technique is frequently exploited predominantly due to the complexity of the ice mixtures investigated. Such complex mixtures result in the overlap of IR bands, making it difficult to distinguish the features. Especially in a polar ice, IR bands typically broaden, which can then hide other features of interest. This lack in distinction is usually not as severe in TPD experiments, as will be discussed in the following paragraphs. Additionally, the detection limit of the QMS on SURFRESIDE³ is around 0.005 monolayers,

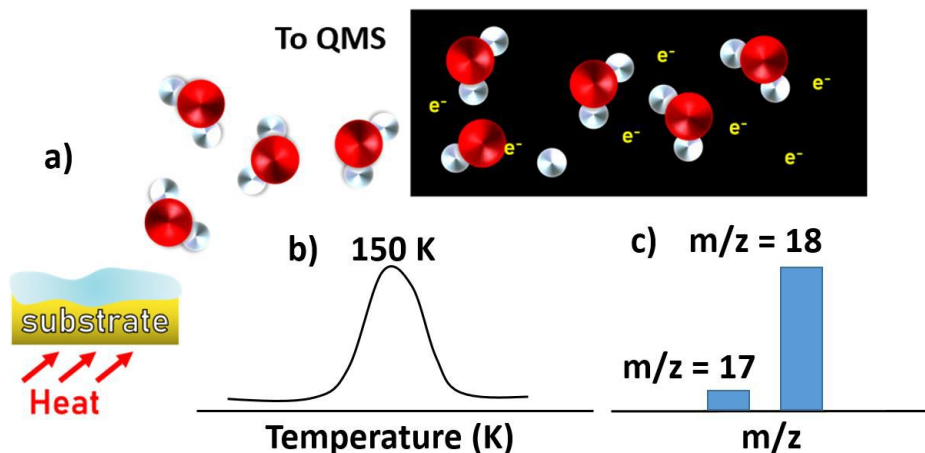


Figure 2.3: Illustration of the basic concept of a TPD experiment (a) and the two molecule-specific parameters typically probed by this method: the desorption temperature and profile (b) and the fragmentation pattern (c).

whereas the FTIR has a detection limit around an order of magnitude less (for species with large band strengths), making TPD a useful technique for probing the COMs that are not abundantly formed.

The basic idea behind a TPD experiment and the information it can provide to constrain the composition of an ice matrix are shown in Figure 2.3. As displayed in Figure 2.3 a, a controlled heat source is used to warm the ice so that the molecules desorb on a linear timescale. This linearity is necessary, as molecules desorb at specific temperatures (e.g., Figure 2.3 b). Some of these molecules will enter the ionization source of the QMS and become ionized and even fragment by accelerated electrons that are emitted from a heated cathode. Since every molecule has a characteristic fragmentation pattern, such a pattern acts as a fingerprint of the dissociated molecule (e.g., Figure 2.3 c). This pattern can be compared to the standards provided in the NIST database¹, or even better, to the standards measured within the same setup in which the experiment was performed. To maximize the number of ions formed, an electron energy of 70 eV is commonly used (also by the NIST database). This value is also ideal, as the dependence of the fragmentation pattern on the change in the electron impact energy around ~70 eV is relatively low. These ions eventually make their way to the mass analyzer, which consists of four poles. The two positively and negatively biased poles act as low-mass and high-mass filters, respectively, and thus the quadrupole only allows the target species to go through based on the m/z value. The remaining ions are then detected by a Faraday cup or a secondary electron multiplier. More information on the thermal desorption of ices can be found in the works of Brown & Bolina (2007) and Burke & Brown (2010), for example.

¹ William E. Wallace, director, "Mass Spectra" in NIST Chemistry WebBook, NIST Standard Reference Database Number 69, Eds. P.J. Linstrom and W.G. Mallard, National Institute of Standards and Technology, Gaithersburg MD, 20899, <https://doi.org/10.18434/T4D303>, (retrieved October 2, 2019).

Similar to RAIRS, isotopically-enhanced gases can also be used to constrain the identity of a feature. Returning to Figure 2.3, the desorption temperature of H₂O in a H₂O ice is around 150 K under UHV conditions, and this can be observed by monitoring m/z values of 18 (H₂O) and 17 (OH). Incorporation of H₂¹⁸O will result in the rise of $m/z = 20$ (H₂¹⁸O) and 19 (¹⁸OH) at 150 K, along with a fragmentation pattern that is now shifted to $m/z = 20$ and 19. Repetition of this procedure with 2-3 different isotopically-enhanced gases is ideal to securely constrain the peak's identity.

To use TPD data to identify a species, it is necessary to know what parameters influence the TPD profile and in what ways. The Polanyi-Wigner formula describes the intensity of the desorption peak, under the condition that the rate of desorption is less than the rate of removal of the desorbed species from the UHV chamber. Below shows a simplified version of the formula, as adapted from Kolasinski (2012):

$$I(t) \propto r_{des} = \frac{-d\theta}{dt} = \nu_n \theta^n \exp\left(-\frac{E_{des}}{RT}\right) \quad (5)$$

where r_{des} is the rate of desorption, θ is the surface coverage, t is time, ν is the pre-exponential factor, n is the desorption order, E_{des} is the energy of desorption, R is the gas constant, and T is the substrate temperature. This formula can be coupled with the mathematical description of the desorption process:

$$T = T_0 + \beta t \quad dT = \beta dt \quad dt = \frac{dT}{\beta} \quad (6)$$

where T_0 is the temperature at $t = 0$, and β is the ramp rate. Substitution of $\frac{dT}{\beta}$ in equation 5 results in:

$$\frac{-d\theta}{dt} = \frac{\nu_n \theta^n \exp\left(-\frac{E_{des}}{RT}\right)}{\beta} \quad (7)$$

Since the maximum intensity (i.e., peak desorption temperature) is when the slope of the TPD profile is zero, the derivative of the above formula with respect to temperature can be set to zero in order to determine how the peak desorption temperature is influenced by other parameters. Rearrangement of Equation 7 after setting the derivative to zero results in:

$$\frac{E_{des}}{RT^2} = \frac{\nu_n}{\beta} \exp\left(-\frac{E_{des}}{RT}\right) \quad (8)$$

Thus, the peak desorption temperature is proportional to the heating rate and the desorption energy. Additionally, the ice matrix can also influence the temperature at which molecules desorb. The binding energy of a molecule may shift depending on the ice mixture, which in turn affects the peak desorption temperature. Molecules may also be trapped by less volatile species, resulting in co-desorption (Fayolle et al. 2013, and references therein). It should be noted that the desorption energy and pre-exponential factor can also depend on the coverage of material on the surface.

The TPD method can also provide information on the relative abundances. The general formula is shown below (adapted from Martín-Doménech et al. (2015)):

$$N_{x,y}(\text{mol}_{x,y}) = \frac{A_{x,y}(m/z)}{\sigma_{x,y}^+(\text{mol}_{x,y})I_{F_{x,y}}(z)F_{F_{x,y}}(m)S_{x,y}(m/z)} \quad (9)$$

where x and y represent different molecules, $A(m/z)$ is the integrated QMS area, $\sigma^+(\text{mol})$ is the ionization cross section, $I_F(z)$ is the ionization factor, $F_F(m)$ is the fragmentation factor, and $S_F(m/z)$ is the sensitivity that is calibrated and specific to each mass spectrometer. The sensitivity values for SURFRESIDE are found in Chuang (2018, Univ. Leiden). The relative abundance is calculated by dividing $N_x(\text{mol}_x)$ by $N_y(\text{mol}_y)$.

The RAIR and TPD configurations in SURFRESIDE allow users to combine the two techniques to link the solid-state and gas-phase signatures, which results in a more accurate determination of the ice species formed. A typical procedure is as follows: RAIR spectra are collected during the ice deposition. The ice is then heated using a linear ramp rate (i.e., TPD). During the TPD process, RAIR spectra are collected, which results in RAIR data acquired as a function of the substrate temperature. The gradual disappearance of infrared peaks can be linked to the rise of desorption signals in the TPD, which may ultimately provide more secure assignments for the infrared and mass spectrometry signatures.

2.2 Experimental Setup: Carbon atom source testing chamber

Before implementation of the C-atom source into SURFRESIDE, it was necessary to first test and further optimize the source in a separate testing vacuum chamber. This is because the nature of carbon is not compatible with these types of systems, as carbon can short circuit electronics, attenuate light, create blockage, is difficult to remove, and so on. Moreover, prior to Qasim et al. (2020b), there were no reports (to our knowledge) on the coupling of the SUKO-A 40 source to a UHV setup that contained cryogenic equipment, and thus its behavior under such conditions was unknown. The test setup is shown in Figure 2.4. It is designed to mimic, as close as possible, the conditions of the main chamber of SURFRESIDE. This includes having a base pressure of low $\sim 10^{-9}$ mbar at room temperature, and a gold-plated substrate that reaches a base temperature of 17 K. The horizontal and vertical distances between the carbon filament and the substrate surface are constant between the test setup and that of SURFRESIDE. The details of the C-atom source in SURFRESIDE³ will be addressed in the next sections. Here, a short recap of the preparations needed to realize this implementation into the main setup is given.

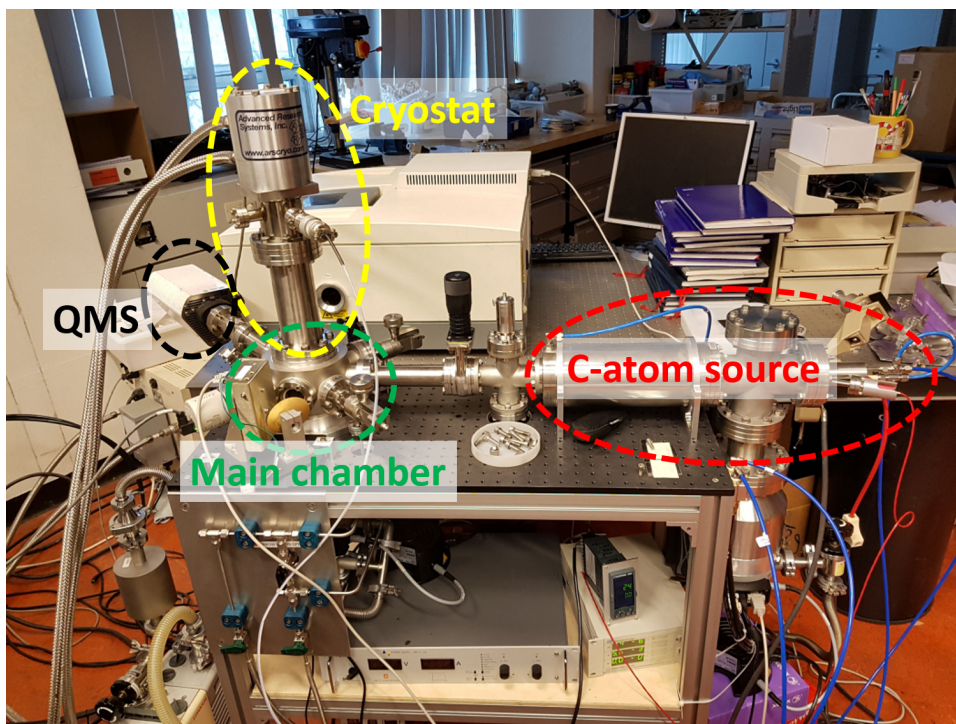


Figure 2.4: The C-atom source testing chamber used to test and optimize the source before its incorporation into SURFRESIDE. Highlighted are the main components, which are the C-atom source (red), the main chamber where ices are grown (green), the cryostat used to create the ices (yellow), and the QMS used to conduct preliminary measurements (black).

One of the main purposes of the testing chamber is to constrain the atomic carbon beam size. Ideally, the beam should not be larger than the substrate surface, but also should cover most of it. This ensures that the components of the main chamber will not be polluted and that carbon chemistry is uniformly distributed on the surface, respectively. To protect the equipment within the test chamber, a long and wide plate is initially used as a substitute for the relatively small gold-plated substrate, as shown in Figure 2.5. As carbon has a high sticking coefficient and is black, the beam size can be directly measured. Copper gaskets with various sized apertures are used to reduce the beam diameter to an ideal value of 21.5 mm, as shown in Qasim et al. (2020b).

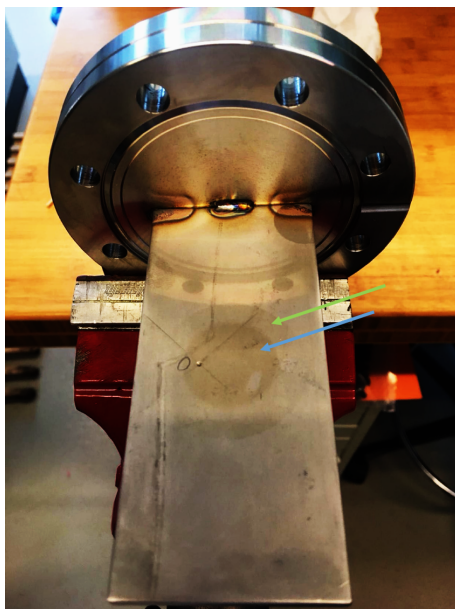


Figure 2.5: Initial results of the atomic carbon beam size using a relatively large plate prior to testing with the gold-plated substrate. The dark circle (blue arrow), with a diameter of 25 mm, represents the majority of the carbon flux. A lighter shaded circle (green arrow), which surrounds the darker shaded circle, is due to residual carbon.

Another main purpose of the testing chamber is to see if solid-state chemistry occurs when using the C-atom source, and under what conditions. These trials are useful, in that experiments can be immediately performed within SURFRESIDE, which limits the atomic carbon pollution in the more expensive apparatus. It is also noted that the survival of the QMS in the testing chamber during an experiment, which is an analytical tool on SURFRESIDE that may be susceptible to short-circuiting by C-atoms, is an important finding. The QMS is positioned in the same geometry with respect to the carbon atom beam as that of SURFRESIDE.

Figure 2.6 shows TPD data of a C + $^{18}\text{O}_2$ co-deposition experiment. The peaks of interest are at 37 and 85 K, which likely represent the desorptions of C^{18}O and C^{18}O_2 , respectively. Note that the desorption temperatures are shifted ~ 5 K higher than expected, and may be due to a miscalibration of the temperature controller. The desorption signal at 37 K for $m/z = 48$ is possibly representative of the co-desorption of C^{18}O_2 with C^{18}O and the contaminant, CO. The formation of C^{18}O and C^{18}O_2 from C + $^{18}\text{O}_2$ is confirmed in Qasim et al. (2020b). Such findings show that the C-source is already optimized to conduct solid-state chemistry that is detectable by TPD-QMS, making it available to incorporate into SURFRESIDE.

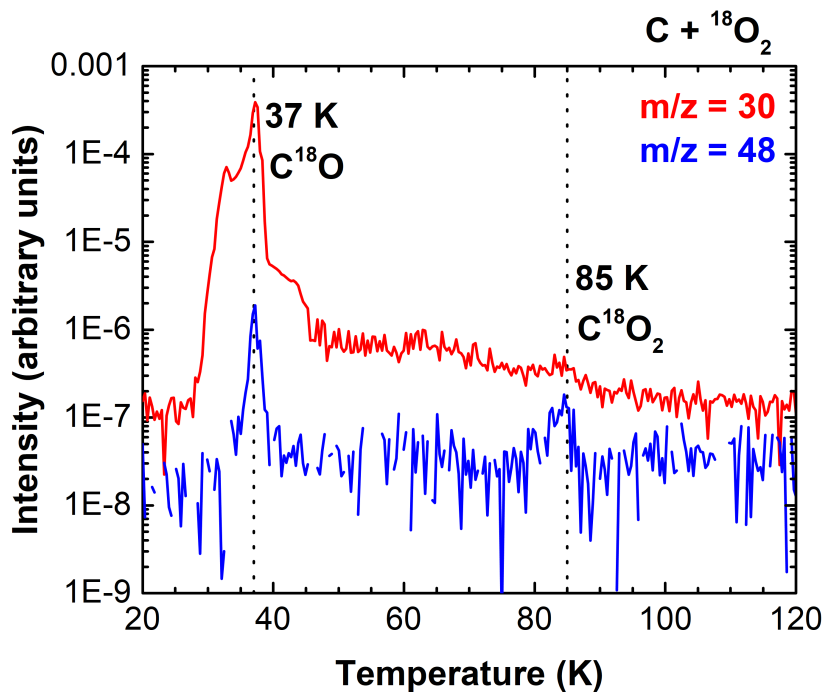


Figure 2.6: TPD-QMS spectra of $C + {}^{18}\text{O}_2$ taken by the testing chamber QMS (Pfeiffer PrismaPlus). Spectra are recorded after ice growth at 17 K. The likely desorptions of $C^{18}\text{O}$ and $C^{18}\text{O}_2$ are shown at 37 and 85 K, respectively. More details on the $C + {}^{18}\text{O}_2$ reaction are found in Gasim et al. (2020b).

2.3 Introduction

The design, implementation, and performance of a customized carbon atom beam source for the purpose of investigating solid-state reaction routes in interstellar ices in molecular clouds are discussed. The source is integrated into an existing ultrahigh vacuum setup, SURFace REaction SIMulation DEvice (SURFRESIDE²), which extends this double atom (H/D, O, and N) beamline apparatus with a third atom (C) beamline to a unique system that is fully suited to explore complex organic molecule solid-state formation under representative interstellar cloud conditions. The parameter space for this system is discussed, which includes the flux of the carbon atoms hitting the ice sample, their temperature, and the potential impact of temperature on ice reactions. Much effort has been put into constraining the beam size to within the limits of the sample size with the aim to reduce carbon pollution inside the setup. How the C-atom beam performs is quantitatively studied through the example experiment, C + ¹⁸O₂, and supported by computationally-derived activation barriers. The potential for this source to study the solid-state formation of interstellar complex organic molecules through C-atom reactions is discussed.

Complex organic molecules (COMs; carbon and hydrogen bearing molecules with at least 6 atoms) have been detected in the cold and lightless environments of prestellar and starless molecular cloud cores (i.e., in the dark interstellar regions which are shrouded by dust), in addition to other astrophysical environments (Herbst & van Dishoeck 2009; Soma et al. 2018; Bacmann et al. 2019). 3-carbon COMs have now been observed in star-forming regions towards both, high-mass (Belloche et al. 2013, 2016) and low-mass (Lykke et al. 2017) sources. Astrochemical models generally assume that a majority of the detected COMs in such surroundings originate from radical-induced surface reactions, in which the radicals are of molecular form (Garrod & Herbst 2006; Vasyunin et al. 2017). This is supported by a series of recent laboratory and theoretical investigations of solid-state reactions, such as HCO, CH₃O and CH₂OH recombinations, in which the radicals are formed by addition and abstraction reactions within the CO hydrogenation route (Chuang et al. 2016; Butscher et al. 2017; Fedoseev et al. 2017; Álvarez-Barcia et al. 2018; Lamberts et al. 2019).

Another solid-state pathway that offers a route to larger COMs is through direct carbon atom chemistry. This route has been proposed in theoretical works (Tielens & Charnley 1997; Charnley 2001a; Charnley & Rodgers 2005, 2009), applied to observational studies (Requena-Torres et al. 2008), and recently in astrochemical models (Simončič et al. 2020). Neutral atomic carbon derived from the gas-phase is one of the most abundant elements in space, (Phillips & Huggins 1981; van Dishoeck et al. 1988; Herbst 2005) and is primarily available during the early period of ice formation (i.e., before it reacts to form CO

gas). (van Dishoeck 1998; Hollenbach et al. 2008; Taquet et al. 2014). The laboratory study of C-atom chemistry under conditions representative for cold molecular clouds (i.e., ground state atomic carbon on 10 K surfaces in an ultrahigh vacuum (UHV) environment) has turned out to be very challenging, as it is experimentally difficult to produce an intense beam of largely ground state atomic carbon. This is a reason why there is little known regarding the role and relevance of C-atom addition reactions in solid-state astrochemical processes. Recent laboratory works have demonstrated how atomic carbon can react to form simple radicals (Krasnokutski et al. 2016; Henning & Krasnokutski 2019) and COMs (Krasnokutski et al. 2017) within liquid helium droplets. The present work extends on this with the first ice system capable to study C-atom chemistry reactions in interstellar ice analogues.

The focus here is on the design, implementation, and characterization of an atomic carbon source into an existing atomic beamline setup, SURFACE REaction SIMulation DEvice (SURFRESIDE²) (Ioppolo et al. 2013), which is dedicated to studying molecular cloud surface reactions. The experimental details of this setup are described elsewhere (Ioppolo et al. 2013). SURFRESIDE² has been used to show how H₂O, CO₂, and COMs can form under interstellar cloud conditions (Ioppolo et al. 2010; Chuang et al. 2016; Fedoseev et al. 2017; Qasim et al. 2019b). The two available atomic beamlines currently permit the formation of a number of radicals, including H/D, N, O, OH, and NH_x. The addition of an atomic carbon source further extends the possibilities to study COM formation by the accretion of atoms and small radicals, which is representative of the low density phase of molecular clouds where atoms are not yet largely locked up into molecules (Linnartz et al. 2015; Boogert et al. 2015).

The original design of the atomic carbon source is found in the work by Krasnokutski & Huisken (2014) and the source discussed in this article is a customized SUKO-A 40 from Dr. Eberl MBE-Komponenten GmbH (MBE), patent number DE 10 2014 009 755 A1. The design of the tantalum tube that is filled with graphite powder can be found in the works by Krasnokutski & Huisken (2014) and Albar et al. (2017). Heating of the tube causes the carbon to sublime and react with the tantalum to produce tantalum carbide, resulting in the conversion of molecular carbon into atomic carbon. Thus, the advantage of this source is that it essentially produces C-atoms rather than C_x clusters (<1% C₂ and C₃ molecules) (Krasnokutski & Huisken 2014). Additionally, carbon atoms are formed by thermal evaporation rather than ‘energetic’ processing. Therefore, we expect the formation of only ground state C(³P) atoms with moderate kinetic energies. The implementation, design, and calibration measurements of the source are described in section 2.4. Its performance, shown through example reactions which are considered relevant from an astronomical perspective and useful for calibration purposes, is presented in section 6.3. The results are interpreted following computationally-calculated activation barriers that are briefly discussed. Section 2.6 discusses how this source can be used to investigate astrochemically relevant surface reactions, and how it can contribute to the science proposed with the upcoming James Webb Space Telescope (JWST). Section 2.7 lists the concluding remarks by summarizing the pros and cons of the new setup described here.

2.4 SURFRESIDE³ and atomic carbon source description

The new C-atom source is implemented into an existing setup, SURFRESIDE², that has been described in detail before (Ioppolo et al. 2013). The extended system, SURFRESIDE³, is shown in the 3D representation of Fig. 2.7. This UHV system allows the growth of interstellar ice analogues on a sample surface for temperatures as low as 8 K using a closed-cycle helium cryostat. It comprises of three atomic beam lines. The HABS and MWAS beamlines have angles of 45° to surface normal of the sample. The C-atom source is mounted in between the HABS and MWAS, and faces the plane of the surface of the ice substrate perpendicularly. The result of impacting H/D-atoms by the Hydrogen Atom Beam Source (HABS) (Tschersich & Von Bonin 1998; Tschersich 2000; Tschersich et al. 2008), and/or H/D-, O-, N-atoms, and molecular radicals by the Microwave Atom Source (MWAS; Oxford Scientific Ltd.), and/or C-atoms by the new C-atom source is monitored using reflection-absorption infrared spectroscopy (RAIRS) and/or temperature programmed desorption-quadrupole mass spectrometry (TPD-QMS). RAIRS allows monitoring of the formation of reaction products *in situ*, as well as quantitative measurements of the newly formed products using a Fourier Transform Infrared Spectrometer (FTIR). TPD-QMS is complementary to RAIRS, as it exploits the desorption temperature, mass-to-charge (m/z) value, and electron impact induced fragmentation pattern of the desorbed species to identify newly formed ice products. SURFRESIDE³ is unique, as it allows to operate three different atomic beam lines simultaneously.

Ices are grown on the gold-plated substrate that is positioned vertically in the center of the main chamber of SURFRESIDE³, which reaches a base pressure of $\sim 3 - 4 \times 10^{-10}$ mbar at the start of each experiment. The surface is positioned such that it directly faces the C-atom source beam. A substrate temperature range of 8 - 450 K is achieved by usage of a closed-cycle helium cryostat and resistive heating. The substrate temperature is probed by a silicon diode sensor that has an absolute accuracy of 0.5 K.

2.4.1 Design of the C-atom line

Fig. 2.8 illustrates the cross section of the C-atom source stainless steel chamber, which has a base pressure of $\sim 2 \times 10^{-9}$ mbar when the source is at its standby current of 40 A. Two water-cooled power contacts are used to heat the source by means of a DC power supply that produces up to 1500 W (Delta Elektronika, SM 15-100).

The source is inserted into the vacuum chamber through a 4-way cross (CF 63). At the bottom of the cross hangs a turbomolecular pump attached to an adapter (Leybold 350i, 290 l/s for N₂, CF 100). As shown in Fig. 2.8, the pump is placed behind the source to keep the pump at a distance from the carbon atom beam, as carbon deposits may stick and potentially harm the pump blades by applying weight to them. A water-cooled shroud is attached to the right flange of the 4-way CF 63 cross to prevent surrounding components from melting, as operating temperatures are around 2030°C. A tantalum shield

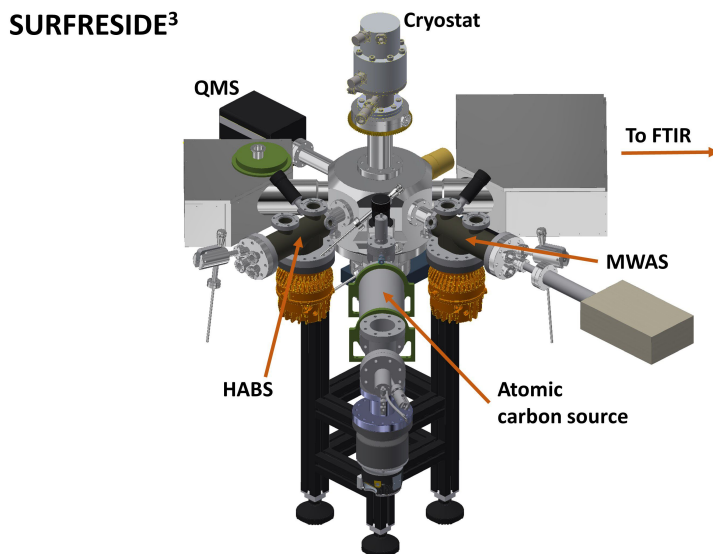


Figure 2.7: A three atomic beam line system, including the new C-atom source introduced here. The three atomic beam lines are capable of generating, H/D, N, O, and C-atoms, in addition to small radicals (e.g., OH, NH). It also contains two regular deposition lines. Both, pre-deposition and co-deposition experiments can be performed. RAIRS and TPD-QMS are used as diagnostic tools.

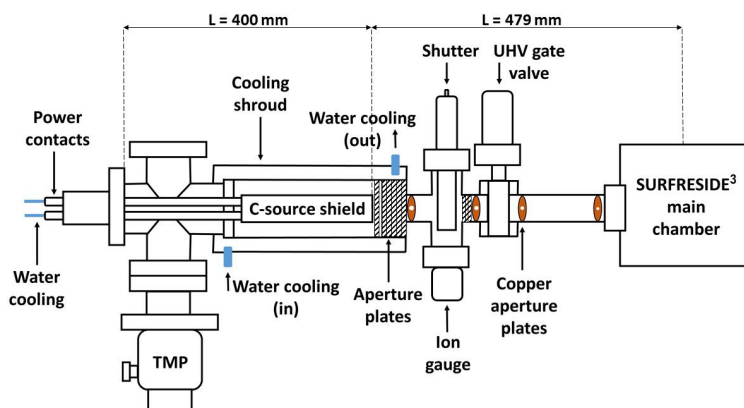


Figure 2.8: Side view schematic of the atomic carbon source vacuum chamber.

is placed around the C-atom source for further protection. To the right of the shroud is a 4-way CF 40 cross piece. The top flange of the cross is attached to a rotary shutter. This shutter is situated in between the path of the emitting carbon atoms and the mini UHV gate valve in order to protect the gate valve from carbon build-up during ramping of the current. The gate valve is installed for the purpose of separating the C-atom source from the main chamber when necessary. At the bottom of the cross hangs a micro-ion gauge (Granville-Phillips, 355001-YG). Various sized aperture plates are installed to spatially restrict the carbon atom beam, where more details are found in section 2.4.2.

Unlike the HABS and MWAS, the exit of the C-source does not have a nose-shaped quartz tube to help collisionally thermalize newly formed atoms before they impact the ices that are on top of the substrate; C-atoms have a much higher sticking coefficient and would coat the tube effectively with a carbon layer. This means that the impacting C-atoms carry the potential to induce thermal processing of the ice, which would not be representative of interstellar conditions. This is an important issue that has been addressed in more detail in the first science result with this new source; in Qasim et al. (2020a) it was demonstrated that in a $C + H + H_2O$ experiment – combining the HABS and C-atom source – the barrierless formation of CH_4 at 10 K predominantly follows a Langmuir-Hinshelwood mechanism (i.e., diffusing reactants thermalize prior to reaction on the surface). This suggests the likelihood of thermalization of the involved reactants, but it is not secured as to whether C-atoms thermalize with the substrate prior to reaction, as the formation of CH in the $C + H + H_2O$ experiment may also proceed by Eley-Rideal (i.e., one reactant is not thermalized prior to reaction). For barrierless reactions, this is not relevant for qualitative studies, as such reactions will proceed regardless of the kinetic energy of the C-atoms. However, for reactions in which a barrier is involved, caution should be taken particularly for quantitative analysis, as the heat of the carbon atoms could open reaction pathways that are not accessible under typical interstellar conditions.

2.4.2 Beam size calibration

The beam size is measured on a gold-decorated substrate that has a width of 24 mm and length of 38 mm, and is positioned at a horizontal distance of 512 mm from the tantalum tube. Fig. 2.9 shows the resulting circular carbon atom beam diameter of 21.5 mm on the gold surface. The beam is narrowed by a combination of stacked oval-like aperture plates (produced by MBE) and circular copper aperture plates (produced in Leiden), as shown in Fig. 2.8. From left to right, the aperture plates by MBE consist of one pyrolytic graphite (PG) plate with an orifice of 18×6 mm, five tantalum plates with an orifice of 19×7 mm, and three tantalum plates with an orifice of 20×12 mm. The PG plate is placed directly after the source to allow the carbon to grow on it without introducing flakes, as thin graphite layers on thin metal parts sometimes create flakes. Multiple plates of the same aperture size are for the purpose of acting as radiation shields. The mean distance between the left-most and right-most aperture plate is 135 mm. The aperture sizes of the copper plates are 21 mm, 20 mm, 19 mm, and 18 mm, respectively, where the plate with the smallest aperture is placed closest to the substrate surface. From left to right,

the distances between the copper plates are 126 mm, 35 mm, and 129 mm. The resulting beam size is optimized in that the majority of the atoms do not go past the sample plate, yet covers a large fraction of the substrate surface in order to have maximum overlap with the FTIR IR beam.



Figure 2.9: The darker circle, outlined by a dashed circle, is carbon deposit that resulted from the atomic beam on the gold surface of the substrate. The entire beam is on the flat surface, and the angle at which the picture is taken makes it appear that the lower part is clipped. A beam diameter of 21.5 mm is measured on a sample plate that has a size of 38 mm \times 24 mm. Note that contrast has been added to the image to visualize the area with impacting C-atoms.

2.4.3 Temperature of the graphite-filled tantalum tube

An approximation for the temperature of the graphite-filled tantalum tube, and consequently of the emitting carbon atoms, is measured by a WRe alloy wire that is largely shielded with Al_2O_3 ceramic. A temperature controller (Eurotherm 2408) is primarily used to read out the temperature value. As the thermocouple is placed beneath the tube to protect it from melting, the measured value from the thermocouple is lower than the actual temperature of the heated tube. To know the actual temperature of the graphite-filled tantalum tube, and subsequently the emitting carbon atoms, a pyrometer is used (at MBE) in conjunction with the thermocouple, and the values are shown in Figure 2.10. Note that the C-atoms are assumed to be in thermal equilibrium with the tantalum tube, although in reality, their temperatures are lower, as the energy required to release the C-atoms from the tube (physisorption/chemisorption) is not taken into account. Interpolation of the values provides the approximate temperature of the carbon atoms for every thermocouple reading from 728 - 1567°C. These gas-phase temperature values are important for determining the flux of carbon

atoms on the sample, as the flux is highly dependent on the filament temperature. Note that the pyrometer values are representative of ground state atomic carbon, as the amount of energy required to reach the $C(^1D)$ excited state is $14,665 \text{ K}^2$.

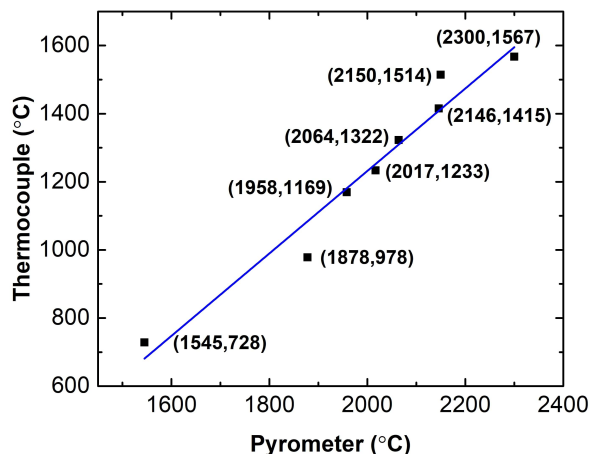


Figure 2.10: A linear fit to the thermocouple versus pyrometer temperature values of the tantalum tube. The values from the pyrometer reflect the approximate C-atom temperatures, whereas the values from the thermocouple are lower due to the distance between the thermocouple and the heated tube.

2.4.4 C-atom flux calibration

In order to characterize the reaction efficiencies in the ice, it is important to quantify the C-atom flux. In Ioppolo et al. (2013), this was demonstrated for the HABS (H/D) and MWAS (H/D, N, O) fluxes. Here, the calibration procedure for the C-atom source is described through a quantitative analysis of various C + $^{18}\text{O}_2$ co-deposition experiments. RAIRS is used to probe and quantitate the reaction products. A wavelength range of $4000\text{--}750 \text{ cm}^{-1}$ with 1 cm^{-1} spectral resolution is used. In section 6.3, it will be explained that C + $^{18}\text{O}_2$ acts in a barrierless manner to ultimately form $C^{18}\text{O} + ^{18}\text{O}$. ^{18}O can then barrierlessly react with $^{18}\text{O}_2$ to form $^{18}\text{O}_3$ (Lin & Leu 1982; Ioppolo et al. 2013). Thus, in a very diluted C: $^{18}\text{O}_2$ matrix of $\sim 1:500$, the $^{18}\text{O}_3$ abundance essentially reflects the C-atom abundance at the substrate. This aimed ratio of 1:500 is determined by estimating the C-atom flux using the C-atom flux values from MBE (application of the inverse-square law), and using the Langmuir approximation ($1 \text{ L} = 1.3 \times 10^{-6} \text{ mbar s} = 1 \times 10^{15} \text{ molecules cm}^{-2}$) to estimate the $^{18}\text{O}_2$ flux. Note that an exact ratio of 1:500 is not critical in these specific experiments,

2 Kramida, A., Ralchenko, Yu., Reader, J., and NIST ASD Team (2018). NIST Atomic Spectra Database (ver. 5.6.1), [Online]. Available: <https://physics.nist.gov/asd> [2019, September 13]. National Institute of Standards and Technology, Gaithersburg, MD. DOI: <https://doi.org/10.18434/T4W30F>

as the main goal is to just create an overabundance of oxygen. Assuming a linear deposition rate, the flux of $^{18}\text{O}_3$, and thus atomic C, can be measured. To calculate the $^{18}\text{O}_3$ abundance, a modified Lambert-Beer equation is used, as employed in previous work (Chuang et al. 2018). A setup specific ozone band strength of 4.4×10^{-17} cm molecule $^{-1}$ is applied, and derived by performance of an isothermal consumption experiment of O_3 by H-atoms at a deposition temperature of 50 K. The H-atom bombardment of O_3 ice at 50 K proceeds via an Eley-Rideal mechanism to form products, such as O_2 , which desorbs upon formation. Thus, the rate of O_3 consumption by H-atoms is directly proportional to the H-atom flux (i.e., linear) until the surface is only partially covered by O_3 . At that point the slope decreases, as the rate of O_3 consumption is hindered by the lack of O_3 at certain binding sites. Thus, the IR absorbance value of O_3 at the transition point is considered to represent a monolayer (ML; 1 ML = 1×10^{15} molecules cm^{-2}) of O_3 ice, and is used to determine the band strength via the modified Lambert-Beer equation. A similar procedure was described in Ioppolo et al. (2013) to determine band strengths with SURFRESIDE².

Table 2.1: The $^{18}\text{O}_3$ (C-atom) flux values at various C-atom temperatures, measured from various C + $^{18}\text{O}_2$ co-deposition experiments. The C: $^{18}\text{O}_2$ ratio is aimed to be $\sim 1:500$ in the experiments. ^aMeasurement performed with another tantalum tube of the same design.

Thermocouple (°C)	Deposition time (s)	$^{18}\text{O}_3$ (C-atom) flux ($\text{cm}^{-2} \text{ s}^{-1}$)
1243	600	1×10^{11}
1287	600	3×10^{11}
1312 ^a	600	4×10^{11}
1325 ^a	600	7×10^{11}
1445	600	3×10^{12}
1533	600	7×10^{12}

The results are summarized in Table 2.1. An exponential curve can be fit to the values in the last column of Table 2.1 in order to indirectly achieve C-atom flux values between thermocouple temperatures of 1243°C and 1533°C. The fluxes at the extremes are also measured by MBE for this particular source with a quartz crystal microbalance, and values of $1 \times 10^{11} \text{ cm}^{-2} \text{ s}^{-1}$ and $1 \times 10^{12} \text{ cm}^{-2} \text{ s}^{-1}$ are obtained for thermocouple temperatures of 1233°C and 1514°C, respectively. These do not deviate much from the values of $1 \times 10^{11} \text{ cm}^{-2} \text{ s}^{-1}$ (1233°C) and $5 \times 10^{12} \text{ cm}^{-2} \text{ s}^{-1}$ (1514°C) obtained with SURFRESIDE³. The $5\times$ deviation in flux at 1514°C can be due to a number of factors, such as the use of different vacuum chamber designs/geometries (including different pumping capacities), filament designs, and measurement tools. It is clear that for the use of this source in experiments for which flux values are needed, it is important to perform a setup specific calibration. Therefore, the method of measuring the $^{18}\text{O}_3$ abundance in an oxygen-rich C + $^{18}\text{O}_2$ co-deposition experiment to determine the C-flux should be repeated if changes are made. Note that the inverse-square law is applied in order to compare flux values

to take properly into account the different distances involved in the two used experimental setups.

2.5 Experimental and computational results

The first results of carbon atom chemistry with the SUKO-A in SURFRESIDE³ are presented below. The two experiments are listed in Table 2.2. These experiments are meant to test the performance of the source by conducting simple reactions that also are considered to be of astrochemical relevancy.

Table 2.2: Description of the performed experiments. Experiment 1 involves co-deposition, and experiment 2 involves pre-deposition. The C-atom fluxes are derived from interpolation of the flux values listed in Table 2.1. The Hertz-Knudsen equation (Kolasinski 2012) is used to determine molecular fluxes. $T_{\text{C-atoms}}$ refers to the temperature probed by the thermocouple. (*) refers to 10 Langmuirs (L).

No.	Exp.	T_{sample} (K)	$T_{\text{C-atoms}}$ (°C)	$\text{Flux}_{\text{C-atoms}}$ ($\text{cm}^{-2}\text{s}^{-1}$)	$\text{Flux } ^{18}\text{O}_3$ ($\text{cm}^{-2}\text{s}^{-1}$)	Time (s)
1	C + $^{18}\text{O}_2$	10	1315	4×10^{11}	8×10^{13}	3000
2	C + $^{18}\text{O}_2$	10	1315	4×10^{11}	*	3000

Isotopically enhanced gas, such as $^{18}\text{O}_2$ (Campro Scientific 97%), is used to distinguish reaction products from possible contaminants. Other gases used are H_2 (Linde 5.0) and D_2 (Sigma-Aldrich 99.96%). $^{18}\text{O}_2$ gas enters the main chamber of SURFRESIDE³ through manually operated leak valves from turbomolecularly pumped dosing lines. Experiments proceed by either a pre deposition or co-deposition manner. In the pre-deposition experiment, molecules are first deposited, followed by C-atom bombardment. In the co-deposition experiments, all species are deposited simultaneously. A major advantage of co-deposition is that product abundance is enhanced due to the constant replenishment of reactants in the ice upper layer. It is also more representative for interstellar processes (Linnartz et al. 2015). Pre-deposition, on the other hand, allows monitoring of the kinetics of formation and consumption of products and reactants, as the initial abundance is known. This method is also preferred when layered ices have to be studied. More detailed information on the application of these two deposition methods can be found in Ioppolo et al. (2014).

Relative molecular abundances are determined by using a modified Lambert-Beer equation, as done previously with the ozone abundance. The infrared band strength of C^{18}O (2086 cm^{-1}) used is $5.2 \times 10^{-17} \text{ cm molecule}^{-1}$ (Chuang et al. 2018). For C^{18}O_2 (2308 cm^{-1}), a band strength of $4.2 \times 10^{-16} \text{ cm molecule}^{-1}$ is used. This value is obtained by multiplying the band strength of $7.6 \times 10^{-17} \text{ cm molecule}^{-1}$, which is from the work by Bouilloud et al. (2015) by a transmission to RAIR setup specific proportionality factor of 5.5, in which the band strength of CO from Chuang et al. (2018) is used.

Fig. 2.11 features the IR signatures of the reaction products of the C + $^{18}\text{O}_2$ co-deposition experiment. Such products are C^{18}O_2 , C^{18}O , and $^{18}\text{O}_3$. Particu-

larly for the formation of $C^{18}O_2$ and $C^{18}O$, there may be more than one pathway to forming these species. Thus, for a more complete understanding of the $C + O_2$ reaction network, relevant computationally-derived activation and reaction energies are needed and are shown in Table 2.3. Connecting these energy values to the experimental results can delineate the product formation pathways.

All the density functional theory (DFT) calculations are performed in a gas-phase model, which can be expected to cover the main effects (Meisner et al. 2017a), using Turbomole (TURBOMOLE 2018), accessed via ChemShell (Sherwood et al. 2003; Metz et al. 2014). The unrestricted M06-2X functional (Zhao & Truhlar 2008) is used in conjunction with the def2-TZVP (Weigend et al. 1998) basis set. The geometry optimizations are carried out at the same level of theory using the DL-Find (Kästner et al. 2009) optimizer interfaced via ChemShell. The connecting first-order saddle points (transition states) are obtained using the dimer method (Henkelman & Jónsson 1999; Kästner & Sherwood 2008). Numerical Hessians in DL-Find are used to characterize the optimized geometries as local minima or transition states. Reported energies include harmonic vibrational zero point energies. Intrinsic reaction coordinate (IRC) (Meisner et al. 2017b; Hratchian & Schlegel 2004) calculations are performed to confirm the connections between the transition states and the local minima. Benchmark calculations are carried out using coupled-cluster level UCCSD(T)-F12 (Adler et al. 2007; Knizia et al. 2009), with a restricted Hartree-Fock reference and cc-PVTZ-F12 (Peterson et al. 2008) basis set in Molpro (Werner et al. 2012).

As demonstrated from the computational work, the reaction of $C + O_2$ barrierlessly leads to the intermediate, linear C-O-O. This process is exothermic by 410 kJ mol^{-1} in comparison to $C + O_2 \rightarrow CO + O$, which has a reaction energy of -372 kJ mol^{-1} . In this context, it is noteworthy that both, C and O_2 , are in their triplet ground states. As they combine to a singlet state, applying spin conservation results in the generated O-atom to also be in its excited singlet state. Thus, if energy is not dissipated into the ice, the overall process to CO formation is thought to be as fast as an actual barrierless reaction (decay of linear C-O-O to $CO + O(^1D)$). CO can also be formed by the barrierless reaction of $C + O_3 \rightarrow CO + O_2$, as listed in Table 2.3. In Fig. 2.12, $^{18}O_3$ is formed by the barrierless reaction of $^{18}O_2 + ^{18}O$, as shown by the increasing signal of $^{18}O_3$. Likely when $^{18}O_2$ becomes limited, $^{18}O_3$ starts to be consumed by C, as shown by the decreasing signal of $^{18}O_3$. Yet in the co-deposition experiment, it is unlikely that $C^{18}O$ is formed from $C + ^{18}O_3$, since the matrix of $^{18}O_2$ hinders the reaction between C and formed $^{18}O_3$.

If energy is dissipated into the ice, which is probable to occur as energy dissipation appears to occur within picoseconds (Arasa et al. 2010; Fredon et al. 2017; Gasim et al. 2019b), linear C-O-O can decay to CO_2 . However, it should be noted that a continuous reaction path to CO_2 is not found in the present computational simulations due to strong multireference character in the wave function, which is why CO_2 formation from $C + O_2$ is noted as tentative in Table 2.3. CO_2 can also be formed by $CO + O(^3P)$, albeit has a high barrier of 25 kJ mol^{-1} , if $O(^3P)$ is in fact formed. $CO + O(^1D)$ is barrierless to CO_2 formation (Talbi et al. 2006). The abundance ratio of 12:1 for $C^{18}O:C^{18}O_2$ measured in experiment 1 shows that $C^{18}O$ is the more favored product, and thus $C^{18}O_2$ formation is relatively inefficient under our experimental conditions

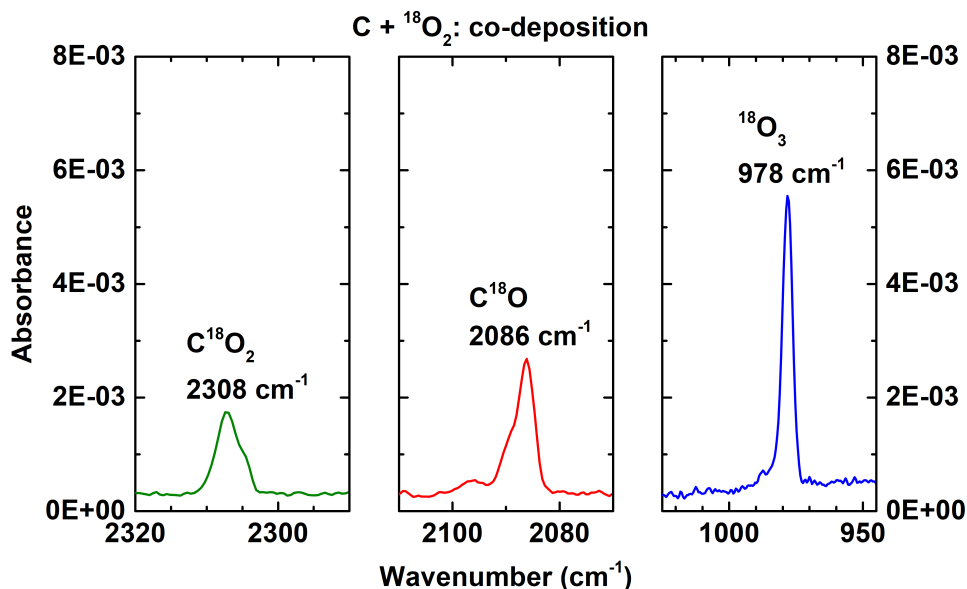


Figure 2.11: A RAIR spectrum acquired after co-deposition of atomic C and $^{18}\text{O}_2$ on a 10 K surface (exp. 1). The features of the reaction products, C^{18}O_2 (left), C^{18}O (middle), and $^{18}\text{O}_3$ (right), are highlighted. A $\text{C}^{18}\text{O}:\text{C}^{18}\text{O}_2$ abundance ratio of 12:1 is measured.

Table 2.3: Activation and reaction energies for $\text{C} + \text{O}_2$, $\text{CO} + \text{O}(^3\text{P})$, $\text{C} + \text{O}_3$, $\text{C} + \text{CO}_2$, and $\text{C}_2\text{O} + \text{CO}$ calculated at the M06-2X/def2-TZVP level of theory. Additionally, a benchmark is performed with the CCSD(T)-F12/VTZ-F12 functional. [1] Formation of the intermediate, linear C-O-O, is further discussed in the main text. [2] Tentative (see main text for more details). [3] Barrierless if energy from the formation of the linear C-O-O intermediate goes into the reaction (see main text for more details).

Reaction	Product(s)	Activation energy (kJ mol^{-1})	Reaction energy (kJ mol^{-1})
$\text{C} + \text{O}_2$ [¹]	$\text{CO} + \text{O}(^1\text{D})$	0[³]	-372
	CO_2 [²]	-	-1106
$\text{CO} + \text{O}(^3\text{P})$	CO_2	25	-527
$\text{C} + \text{O}_3$	$\text{CO} + \text{O}_2$	0	-981
$\text{C} + \text{CO}_2$	$\text{CO} + \text{CO}$	29	-540
$\text{C}_2\text{O} + \text{CO}$	C_3O_2	30	-346

The results of the $\text{C} + ^{18}\text{O}_2$ experiments demonstrate that the C-atom source performs well under our astrochemically relevant experimental conditions to study solid-state reactions. Particularly, the available C-atom flux is sufficient to yield high quality spectra, which allows qualitative and quantitative analysis of the involved chemical pathways.

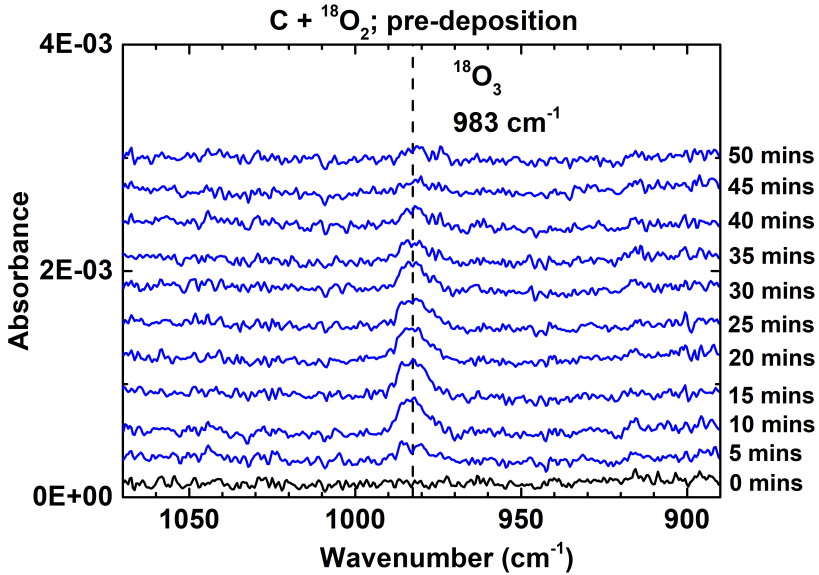


Figure 2.12: RAIR spectra acquired after pre-deposition of atomic C and $^{18}\text{O}_2$ on a 10 K surface (exp. 2). 10 L of $^{18}\text{O}_2$ is first deposited, followed by carbonation for 50 minutes. The increase and subsequent decrease of the $^{18}\text{O}_3$ band is highlighted. RAIR spectra are offset for clarity.

2.6 Astrochemical implications

The new experiments described here are needed to understand how carbonaceous species, and particularly COMs, can be formed by carbon atom chemistry in the early phase of molecular cloud evolution. Such chemistry is expected to be most applicable to the H_2O -rich ice phase, which has a visual extinction (A_V) of $1.5 < A_V < 3$ (Boogert et al. 2015). At such cloud depths, atomic carbon is present, and becomes increasingly locked up in gas-phase CO at greater extinctions ($> 3 A_V$) (van Dishoeck 1998; Boogert et al. 2015). This carbon then has the chance to react with atomic hydrogen on grain surfaces, for example, to form simple species such as CH_4 (Öberg et al. 2008). The intermediate hydrocarbon radicals, CH_x , may also have the opportunity to react with other species in the H_2O -rich ice phase to form COMs. It should be noted that deeper into the cloud when CO freezes-out, C can also be formed by the dissociation of CO by cosmic-ray-induced processes (Herbst & van Dishoeck 2009; Requena-Torres et al. 2008).

The reaction of $\text{C} + \text{O}_2$ in interstellar molecular clouds may occur, as it is demonstrated to be a barrierless reaction, but not expected to be relatively frequent. Although interstellar O_2 ice has not been detected, O_2 has been detected on icy bodies, such as in the coma of comet 67P/Churyumov-Gerasimenko, and is thought to have primordial origin (Bieler et al. 2015; Taquet et al. 2016). As found in Taquet et al. (2016), the distributions of the O_2 ice abundance at $A_V = 2, 4, 6, 8,$ and 10 are similar between the A_V levels. Thus, the astrochemical timescales of relatively abundant C and O_2 should overlap. However, atoms

such as H and O also barrierlessly react with O_2 , and are at least an order of magnitude higher in abundance than C at the same timescales (Hollenbach et al. 2008; Taquet et al. 2014, 2016). Therefore, the reaction of C with O_2 in the translucent and dense phases of interstellar clouds is assumed to be minor for O_2 consumption. Nonetheless, the experimental and theoretical work presented here shows that atomic carbon and molecular oxygen can readily react if they would neighbor each other on a dust grain. The C + O_2 products, CO, and possibly $O(^3P)$ and CO_2 , are unlikely to further react with each other in the laboratory or in the interstellar medium, as such reactions are associated with high activation barriers, as found in Table 2.3. This includes $CO + O(^3P) \rightarrow CO_2$ (25 kJ mol^{-1}), $C + CO_2 \rightarrow CO + CO$ (29 kJ mol^{-1}), and $C_2O + CO \rightarrow C_3O_2$ (30 kJ mol^{-1}). However, the formation of $O(^1D)$ from C + O_2 may explain why CO_2 is formed starting from a ‘non-energetic’ reaction, in which ‘non-energetic’ refers to a radical-induced process that does not include an external energy source such as UV, cosmic rays, electrons, and/or simple heating of the ice. The reaction of C + O_3 is barrierless and thus may also occur in space. However, it is expected to be relatively infrequent for the same reasons as that for the C + O_2 reaction.

The general relevance for the astrochemical community of using a C-atom source in a setup fully optimized to study atom addition/abstraction reactions in interstellar ice analogues is that it extends on reaction networks proposed before (e.g., Charnley & Rodgers (2005)), but has not been investigated in the laboratory yet. It is expected that experimental investigations of solid-state C-atom chemistry will provide some of the missing fingerprints for how different carbon-bearing species are formed in interstellar ices. To date, the formation of solid-state COMs and other carbon-bearing molecules under interstellar relevant conditions is largely investigated through the combination of molecular radicals (e.g., HCO, C_2H_3 , CH_3O), as this way to build the carbon backbone has been experimentally realized for some time. Although it is an important and relevant way to form solid-state carbon-containing species, it is likely not the explanation for the formation of all such species. This is in part due to the presence of atomic carbon in translucent and dense clouds. As atomic C is highly reactive, it may feasibly evolve into C_xH_y structures. These structures can then react with other radicals to form alcohols and aldehydes, as shown in Qasim et al. (2019a) and Qasim et al. (2019b). Alcohols, aldehydes, and other functional groups may also be formed starting from $HCO + C$ (Charnley & Rodgers 2005; Herbst & van Dishoeck 2009) and/or $CCO + H$. Thus, this work will help understand the relative significance of radical recombination and direct C-atom addition reactions in various interstellar molecular cloud environments. For this, also astrochemical modeling will be needed, taking into account the available C-atom abundances in different astronomical environments. With the options SURFRESIDE³ offers, it will become possible to provide information on possible reaction networks and reaction efficiencies and in full dependence of astronomically relevant temperatures.

With the expected launch of the JWST in the near future, ice observations should become more prevalent, which also increases the necessity of laboratory C-atom reactions. To date, telescopes have suffered from telluric contamination (ground-based) and lacked the sensitivity to probe ice molecules more complex than methanol. The JWST will provide telluric free data, sensitivity

and/or spectral resolution in the mid-IR that is orders of magnitude higher than encountered with previous telescopes such as the Infrared Space Observatory (ISO) or Spitzer (Martínez-Galarza et al. 2012), and perform ice mapping. These traits alone make the JWST a desired facility for ice observations, and preparations to search for COMs have already been carried out in the laboratory (Terwisscha van Scheltinga et al. 2018). As possible COMs from C-atom chemistry are expected to be formed primarily in the H₂O-rich ice phase, and not in the CO-rich ice phase, C-atom chemistry experiments may provide insight into the origin of the COMs that will be targeted by the JWST. For example, a COM that is effectively formed by C-atom chemistry, but not by other studied pathways, suggests that the detected COM is formed in the polar phase of the cloud. Currently, not even methanol has been directly and exclusively detected in this phase in quiescent clouds (see Figure 7 of Boogert et al. (2015)), and this is a consequence of the relatively low amount of ice at such low extinctions ($A_V < 3$). Thus, this is the ideal time period to investigate C-atom chemistry, as the JWST may have the sensitivity to detect COMs directly in the polar phase that are formed starting from atomic C.

2.7 Conclusions

For the first time, an atomic carbon source capable of producing fluxes in the low 10^{11} – high 10^{12} cm⁻² s⁻¹ range is incorporated into a modified setup that is designed to study the ‘non-energetic’ chemical processes of interstellar ice analogues. The source comes with new advantages: 1) An alternative way to investigate carbon chemistry in space along a principle that has not been studied so far. 2) A reliable and straightforward method to calibrate the C-atom flux in SURFRESIDE³ is available. The flux is adequate to probe C-atom chemistry in SURFRESIDE³, such as the reaction of C + ¹⁸O₂. The experimental results and computationally-derived activation barriers suggest that atomic carbon can react with O₂ and O₃ ice in interstellar molecular clouds, although more abundant species will effectively compete with C. 3) The beam size can be directly measured, which makes it achievable to operate the source without inducing hazardous carbon pollution into the vacuum system. The use of the source also comes with challenges to keep in mind: 1) The production of carbon layers on the sample surface is unavoidable in an experiment (i.e., all experiments take place on a carbonaceous surface). However, the layers observed have a negligible effect on the RAIR intensity. 2) The flux is highly dependent on the filament temperature, and the filament temperature steadily changes within an experiment partially due to the ongoing release of C-atoms. Thus, the longer the experiment, the greater the deviation of the flux between the start and the end of the experiment. 3) On average, the lifetime of a tube is around 14 hours at thermocouple temperatures of around 1300°C. This complicates experiments due to the necessary replacement of the tube, which can be expensive. 4) The extent of thermalization of the C-atoms to the temperature of the substrate is not fully secured yet, and therefore C-atom reactions involving activation barriers require caution, particularly if quantitative analysis is performed. Future studies will focus on developing a method to measure the extent at which C-atoms thermally equilibrate with the sample.

With the positive performance of the modified setup, it is now possible to test what type of COMs can be formed by C-atom chemistry, primarily in a H₂O-rich ice, as these type of COMs are thought to be mixed primarily with H₂O (and also some CO). Such investigations overlap well with the expected launch of the JWST, which will have a sensitivity in the mid-IR that can possibly pick up signatures of COMs formed in low extinction ($A_V \sim 2$ -3) environments directly – something that has yet to be conducted with current observational facilities.

Bibliography

- Adler, T. B., Knizia, G., & Werner, H.-J. 2007, *J. Chem. Phys.*, 127, 1
- Albar, J., Summerfield, A., Cheng, T. S., et al. 2017, *Sci. Rep.*, 7, 6598
- Álvarez-Barcia, S., Russ, P., Kästner, J., & Lamberts, T. 2018, *Mon. Not. R. Astron. Soc.*, 479, 2007
- Arasa, C., Andersson, S., Cuppen, H., van Dishoeck, E. F., & Kroes, G.-J. 2010, *J. Chem. Phys.*, 132, 1
- Bacmann, A., Faure, A., & Berteaud, J. 2019, *ACS Earth Space Chem.*
- Belloche, A., Müller, H., Garrod, R., & Menten, K. 2016, *Astron. Astrophys.*, 587, A91
- Belloche, A., Müller, H. S., Menten, K. M., Schilke, P., & Comito, C. 2013, *Astron. Astrophys.*, 559, A47
- Bieler, A., Altwegg, K., Balsiger, H., et al. 2015, *Nature*, 526, 678
- Boogert, A., Gerakines, P. A., & Whittet, D. C. 2015, *Annu. Rev. Astron. Astrophys.*, 53, 541
- Bouilloud, M., Fray, N., Bénilan, Y., et al. 2015, *Mon. Not. R. Astron. Soc.*, 451, 2145
- Brown, W. A. & Bolina, A. S. 2007, *Mon. Not. R. Astron. Soc.*, 374, 1006
- Burke, D. J. & Brown, W. A. 2010, *Phys. Chem. Chem. Phys.*, 12, 5947
- Butscher, T., Duvernay, F., Rimola, A., Segado-Centellas, M., & Chiavassa, T. 2017, *Phys. Chem. Chem. Phys.*, 19, 2857
- Charnley, S. 2001a, in *The bridge between the Big Bang and Biology: Stars, Planetary Systems, Atmospheres, Volcanoes: their Link to Life*, ed. F. Giovannelli, 139–149
- Charnley, S. & Rodgers, S. 2005, *Proceedings of the International Astronomical Union*, 1, 237
- Charnley, S. & Rodgers, S. 2009, in *Bioastronomy 2007: Molecules, Microbes and Extraterrestrial Life*, ed. K. Meech, J. Keane, M. Mumma, J. Siefert, & D. Werthimer, Vol. 420, 29–34
- Chuang, K. 2018, *Univ. Leiden, PhD thesis*
- Chuang, K.-J., Fedoseev, G., Ioppolo, S., van Dishoeck, E. F., & Linnartz, H. 2016, *Mon. Not. R. Astron. Soc.*, 455, 1702
- Chuang, K.-J., Fedoseev, G., Qasim, D., et al. 2018, *Astrophys. J.*, 853, 1
- Fayolle, E. C. et al. 2013, *PhD thesis, Leiden Observatory, Faculty of Science, Leiden University*
- Fedoseev, G., Chuang, K.-J., Ioppolo, S., et al. 2017, *Astrophys. J.*, 842, 1
- Fredon, A., Lamberts, T., & Cuppen, H. 2017, *Astrophys. J.*, 849, 1
- Friedbacher, G. & Bubert, H. 2011, *Surface and Thin Film Analysis: A Compendium of Principles, Instrumentation, and Applications* (John Wiley & Sons)
- Fuchs, G., Cuppen, H., Ioppolo, S., et al. 2009, *Astron. Astrophys.*, 505, 629
- Garrod, R. T. & Herbst, E. 2006, *Astron. Astrophys.*, 457, 927
- Harrison, I. 2013, *Why is there a need for UHV?*, <http://faculty.virginia.edu/harrison/STM/tutorials/UHV.html/>, [Online; accessed 03-October-2019]
- Henkelman, G. & Jönsson, H. 1999, *J. Chem. Phys.*, 111, 7010
- Henning, T. K. & Krasnokutski, S. A. 2019, *Nat. Astron.*, 3, 1

- Herbst, E. 2005, *J. Phys. Chem. A*, 109, 4017
- Herbst, E. & van Dishoeck, E. F. 2009, *Annu. Rev. Astron. Astrophys.*, 47, 427
- Hollenbach, D., Kaufman, M. J., Bergin, E. A., & Melnick, G. J. 2008, *Astrophys. J.*, 690, 1497
- Hratchian, H. P. & Schlegel, H. B. 2004, *J. Chem. Phys.*, 120, 9918
- Humblot, V. & Pradier, C.-M. 2011, in *Biointerface Characterization by Advanced IR Spectroscopy* (Elsevier), 1–26
- Ioppolo, S., Cuppen, H., Romanzin, C., van Dishoeck, E. F., & Linnartz, H. 2010, *Phys. Chem. Chem. Phys.*, 12, 12065
- Ioppolo, S., Fedoseev, G., Lamberts, T., Romanzin, C., & Linnartz, H. 2013, *Rev. Sci. Instrum.*, 84, 1
- Ioppolo, S., Öberg, K., & Linnartz, H. 2014, in *Laboratory astrochemistry: from molecules through nanoparticles to grains*, ed. S. Schlemmer, T. Giesen, & H. Mutschke (John Wiley & Sons), 289–309
- Kästner, J., Carr, J. M., Keal, T. W., et al. 2009, *J. Phys. Chem. A*, 113, 11856
- Kästner, J. & Sherwood, P. 2008, *J. Chem. Phys.*, 128, 014106
- Knizia, G., Adler, T. B., & Werner, H.-J. 2009, *J. Chem. Phys.*, 130, 1
- Kolasinski, K. W. 2012, *Surface science: foundations of catalysis and nanoscience* (West Chester, PA: John Wiley & Sons)
- Krasnokutski, S., Goulart, M., Gordon, E., et al. 2017, *Astrophys. J.*, 847, 89
- Krasnokutski, S. & Huisken, F. 2014, *Appl. Phys. Lett.*, 105, 113506
- Krasnokutski, S., Kuhn, M., Renzler, M., et al. 2016, *Astrophys. J. Lett.*, 818, L31
- Lamberts, T., Markmeyer, M. N., Kolb, F. J., & Kästner, J. 2019, *ACS Earth Space Chem.*, 3, 958
- Lin, C. & Leu, M. 1982, *Int. J. Chem. Kinet.*, 14, 417
- Linnartz, H., Ioppolo, S., & Fedoseev, G. 2015, *Int. Rev. Phys. Chem.*, 34, 205
- Lykke, J. M., Coutens, A., Jørgensen, J. K., et al. 2017, *Astron. Astrophys.*, 597, 1
- Martín-Doménech, R., Manzano-Santamaría, J., Caro, G. M., et al. 2015, *Astron. Astrophys.*, 584, 1
- Martínez-Galarza, J. R. et al. 2012, PhD thesis
- Meisner, J., Lamberts, T., & Kästner, J. 2017a, *ACS Earth Space Chem.*, 1, 399
- Meisner, J., Markmeyer, M. N., Bohner, M. U., & Kaestner, J. 2017b, *Phys. Chem. Chem. Phys.*, 19, 23085
- Metz, S., Kästner, J., Sokol, A. A., Keal, T. W., & Sherwood, P. 2014, *Wiley Interdiscip. Rev. Comput. Mol. Sci.*, 4, 101
- Öberg, K. I., Boogert, A., Pontoppidan, K. M., et al. 2008, *Astrophys. J.*, 678, 1032
- Palumbo, M. E., Baratta, G. A., Collings, M. P., & McCoustra, M. R. 2006, *Phys. Chem. Chem. Phys.*, 8, 279
- Peterson, K. A., Adler, T. B., & Werner, H.-J. 2008, *J. Chem. Phys.*, 128, 01
- Phillips, T. & Huggins, P. 1981, *Astrophys. J.*, 251, 533
- Qasim, D., Fedoseev, G., Chuang, K. J., et al. 2020a, An experimental study of the surface formation of methane in interstellar molecular clouds
- Qasim, D., Fedoseev, G., Chuang, K.-J., et al. 2019a, *Astron. Astrophys.*, 627, A1
- Qasim, D., Fedoseev, G., Lamberts, T., et al. 2019b, *ACS Earth Space Chem.*, 3, 986
- Qasim, D., Witlox, M. J. A., Fedoseev, G., et al. 2020b, A cryogenic ice setup to simulate carbon atom reactions in interstellar ices
- Requena-Torres, M., Martín-Pintado, J., Martín, S., & Morris, M. 2008, *Astrophys. J.*, 672, 352
- Sherwood, P., de Vries, A. H., Guest, M. F., et al. 2003, *J. Mol. Struct.: THEOCHEM*, 632, 1
- Simončič, M., Semenov, D., Krasnokutski, S., Henning, T., & Jäger, C. 2020, Sensitivity of gas-grain chemical models to surface reaction barriers: Effect from a key carbon-

- insertion reaction, $C + H_2 \rightarrow CH_2$
- Soma, T., Sakai, N., Watanabe, Y., & Yamamoto, S. 2018, *Astrophys. J.*, 854, 116
- Talbi, D., Chandler, G., & Rohl, A. 2006, *Chem. Phys.*, 320, 214
- Taquet, V., Charnley, S. B., & Sipilä, O. 2014, *Astrophys. J.*, 791, 1
- Taquet, V., Furuya, K., Walsh, C., & van Dishoeck, E. F. 2016, *Mon. Not. R. Astron. Soc.*, 462, S99
- Terwisscha van Scheltinga, J., Ligterink, N., Boogert, A., van Dishoeck, E. F., & Linnartz, H. 2018, *Astron. Astrophys.*, 611, A35
- Tielens, A. & Charnley, S. 1997, in *Planetary and Interstellar Processes Relevant to the Origins of Life* (Springer), 23–51
- Tschersich, K. 2000, *J. Appl. Phys.*, 87, 2565
- Tschersich, K., Fleischhauer, J., & Schuler, H. 2008, *J. Appl. Phys.*, 104, 1
- Tschersich, K. & Von Bonin, V. 1998, *J. Appl. Phys.*, 84, 4065
- TURBOMOLE. 2018, V7.0.01, a development of University of Karlsruhe and Forschungszentrum Karlsruhe GmbH, 1989-2007, TURBOMOLE GmbH, since 2007; available from <http://www.turbomole.com>.
- van Dishoeck, E. F. 1998, in *The Molecular Astrophysics of Stars and Galaxies*, ed. T. Hartquist & D. Williams (Oxford: Clarendon Press), 53
- van Dishoeck, E. F., Black, J. H., et al. 1988, *Astrophys. J.*, 334, 771
- Vasyunin, A. I., Caselli, P., Dulieu, F., & Jiménez-Serra, I. 2017, *Astrophys. J.*, 842, 33
- Weigend, F., Häser, M., Patzelt, H., & Ahlrichs, R. 1998, *Chem. Phys. Lett.*, 294, 143
- Werner, H., Knowles, P., Knizia, G., Manby, F., & Schütz, M. 2012, *Mol. Sci.*, 2, 242
- Zhao, Y. & Truhlar, D. G. 2008, *Theor. Chem. Acc.*, 120, 215